

Substitution of Sr into the Na Layer Elevates the High Voltage Stability of O3-Type NaCrO_2 as Sodium-Ion Battery Cathode

Gwangeon Oh, Yunjae Oh, Shivam Kansara, Heesung Shin, Hyokyeong Kang, Tae-Hoon Kim, Dominic Bresser, and Jang-Yeon Hwang*

Herein, the substitution strategy of Sr^{2+} into Na sites is proposed and its important role in improving the high-voltage stability of O3-type NaCrO_2 cathode (O3-NCO) for high-energy sodium-ion batteries (SIBs) is systematically analyzed. Sr^{2+} possesses similar physicochemical characteristics to that of Na^+ ; hence, Sr^{2+} can preferentially occupy the NaO_6 octahedral sites in O3-NCO, with one Sr^{2+} ion replacing two Na^+ ions. The introduction of Sr^{2+} generates sodium vacancies in the Na^+ layer to compensate for charge neutrality, which facilitates the Na^+ diffusion kinetics. Additionally, Sr^{2+} exhibits electrochemical inactivity and strongly interacts with O^{2-} ions, which triggers the smooth atomic rearrangement related to the sequential phase transformation of O3-NCO at high charging potentials. For the charge–discharge process in a wide operating voltage window (1.5–3.8 V vs. Na/Na^+), the optimal substitution level of 4 mol% substantially suppresses the extent of irreversible phase transition of O3-NCO; as a result, compared to O3-NCO, the O3-type $\text{Na}_{0.92}\text{Sr}_{0.04}\text{CrO}_2$ (O3-NS4CO) cathode demonstrates the superior discharge capacity with stable Coulombic efficiency, long-term cycling stability, and advanced power capability. Furthermore, O3-NS4CO demonstrates excellent practical applicability in pouch-type full cells constructed using a hard carbon anode.


considerations have prompted a shift toward cleaner and more sustainable forms of energy, such as renewable energy for powering electric vehicles.^[3] Lithium-ion batteries (LIBs) are widely used in portable devices, electric vehicles, and stationary energy storage devices.^[4,5] However, LIBs are no longer a permanently available energy source owing to the uneven distribution and scarcity of lithium resources in Earth's crust.^[6] Consequently, various advanced energy storage devices have been developed as complementary technologies to LIBs. Among them, sodium-ion batteries (SIBs) have significant potential as cost-effective and sustainable energy storage systems owing to their operating mechanism, which is similar to that of LIBs, and the abundance of sodium.^[7–11] Diverse SIB cathode materials such as layered oxides, Prussian blue analogs, and polyanionic compounds have been reported.^[12–22] Among many potential cathode materials, layered oxide offers the following comprehensive advantages: 1) high specific capacity; 2) high-rate capability (2D- Na^+ diffusion path); and 3) relatively easier synthesis and manufacturing process. In particular, sodium layered oxides (Na_xTMO_2 ; TM = transition metal) are mainly classified into two categories: O3 and P2. In the O3

1. Introduction

The demand for electric vehicle and energy storage materials is rapidly increasing due to achieving carbon neutrality.^[1,2] These

G. Oh, Y. Oh, S. Kansara, H. Shin, H. Kang, J.-Y. Hwang
Department of Energy Engineering
Hanyang University
Seoul 04763, Republic of Korea
E-mail: jangyeonhw@hanyang.ac.kr

T.-H. Kim
Department of Materials Science and Engineering
Chonnam National University
Gwangju 61186, Republic of Korea

 The ORCID identification number(s) for the author(s) of this article can be found under <https://doi.org/10.1002/sstr.202400561>.

© 2025 The Author(s). Small Structures published by Wiley-VCH GmbH. This is an open access article under the terms of the Creative Commons Attribution License, which permits use, distribution and reproduction in any medium, provided the original work is properly cited.

DOI: 10.1002/sstr.202400561

D. Bresser
Helmholtz Institute Ulm (HIU)
Helmholtzstrasse 11, 89081 Ulm, Germany

D. Bresser
Karlsruhe Institute of Technology (KIT)
P.O. Box 3640, 76021 Karlsruhe, Germany

J.-Y. Hwang
Department of Battery Engineering
Hanyang University
Seoul 04763, Republic of Korea

structure, Na ions are located in octahedral sites and the oxygen stacking order is “ABCABC”, whereas in the P2 configuration, Na ions coordinate in a trigonal prismatic environment and the stacking order of oxygen follows the “ABBA” sequence.^[23] The O3 type cathodes, as Na reservoir, can be matched with carbonaceous anode to manufacture practical Na ion full cells following a similar chemistry to LIBs; therefore, they are considered the most suitable commercial cathode candidate in SIBs.^[24–26]

Among the various O3-type sodium layered oxides, NaCrO₂ has attracted widespread research attention owing to its high theoretical capacity, rate capability, and thermal stability.^[27,28] However, it should be noted that most reported O3-NaCrO₂ can only deliver a limited capacity of $\approx 120 \text{ mAh g}^{-1}$ within a narrow voltage window of 2.0–3.6 V.^[29] Because NaCrO₂ undergoes a reversible hexagonal O3-monoclinic O'3–monoclinic P'3 phase transition only within this limited potential range, providing satisfactory electrochemical performance. On the other hand, further extraction of Na ions (charging over 3.6 V) results in structural degradation accompanied by the irreversible migration of Cr ions from the TM layer to the Na layer, eventually obstructing diffusion channels and reducing the degree of Na insertion.^[30,31] Therefore, stabilization of the crystal structure by suppressing the irreversible migration of Cr ions is key to improving the electrochemical properties of O3-NaCrO₂.^[32,33] To enhance structural stability at potentials above 3.6 V, cationic substitution and carbon coating have been proposed as strategies.^[27,34] For instance, the introduction of strongly bonded active/inactive cations (for example, Nb, Sb, Ti, and Mn) can affect the local electronic environment of the TM layer, thereby reducing changes in lattice parameters, suppressing irreversible phase transitions, and improving the high-voltage stability of the cathode material.^[35–38] However, recent studies have shown that random Na extraction and the formation of Na-deficient layer at a high state of charge are driving forces for TM migration.^[39] Obrovac^[34] and Hwang's group^[40] proposed the introduction of size-matched Ca²⁺ ions into the Na layer to improve structural stability and suppress irreversible phase transitions at high charging cut-off potentials; the resulting Ca²⁺-substituted cathode materials exhibited significantly improved cycling stability. Although the strong net-effective charge of Ca–O bonds is believed to enhance cycling stability owing to the improvement in structural stability, this approach remains inadequate for simultaneously improving the power capability. Hence, NaCrO₂ must be further optimized to achieve high-energy and high-power capabilities along with cycling stability, particularly by mitigating the irreversible migration of Cr ions.

In this study, we first introduced Sr ion into Na site to improve both the high-voltage structural stability and power capability of O3-NaCrO₂. The Sr ions are incorporated into octahedrally coordinated Na⁺ layers, generating sodium vacancies in the Na layer. Owing to the strong interaction between Sr²⁺ and O^{2–}, the high-voltage structural stability of NaCrO₂ was considerably improved.^[34,40] Consequently, O3-Na_{0.92}Sr_{0.04}CrO₂ demonstrated reversible O3-O'3–P'3–O'3–O3 phase transitions, with smaller volume changes than those of O3-NaCrO₂, within a wide operating voltage range of 1.5–3.8 V. Furthermore, O3-Na_{0.92}Sr_{0.04}CrO₂ exhibited a high specific capacity of 130 mAh g^{-1} at 12 mA g^{-1} , an improved capacity retention rate (75% after 1000 cycles at 10 C), and enhanced rate capability with

54% capacity retention at 50 C. More importantly, a pouch-type full cell assembled using a hard carbon (HC) anode and the optimized cathode exhibited outstanding cycling stability (67% capacity retention after 250 cycles at 0.5 C).

2. Result and Discussion

2.1. Material Characterization

A series of Na_{1–2x}Sr_xCrO₂ ($x = 0, 0.02, 0.04, 0.06$) were prepared using a typical solid-state method.^[40] The chemical composition of the samples was determined by inductively coupled plasma-optical emission spectroscopy (ICP-OES) analysis (Table S1, Supporting Information), and the results were consistent with the target compositions. The X-ray diffractometry (XRD) patterns of the cathodes and their Rietveld refinement data confirmed that all diffraction peaks corresponded to the simulated O3-phase crystal structure belonging to the $R\bar{3}m$ space group (Figure 1a,b, and S1, S2, Supporting Information), indicating that Sr is preferentially substituted into the Na layer and does not form impurities by occupying Cr sites. Hereafter, NaCrO₂, Na_{0.96}Sr_{0.02}CrO₂, Na_{0.92}Sr_{0.04}CrO₂, and Na_{0.88}Sr_{0.06}CrO₂ are denoted as O3-NCO, O3-NS2CO, O3-NS4CO, and O3-NS6CO, respectively. As the extent of Sr substitution into the crystal structure increased from 0 to 0.04, the value of the lattice parameter *c* increased monotonically (Table S2, Supporting Information), presumably owing to the increase in the NaO₂ interlayer spacing rather than the compensating effect against the decrease in the CrO₂ interlayer spacing.^[41] The widened NaO₂ interlayer spacing was mainly induced by the enhancement in electrostatic repulsion between oxygen layers (O^{2–}–O^{2–}), as the vacancies were produced in the Na layers by the Sr substitution. The introduction of vacancies in Na layer induced the expanded Na-ion diffusion channel and thus reduces the ionic migration barrier during charge–discharge process.^[42] When 6 mol% Sr was introduced into the Na layers, a peak representing a small fraction of SrCr₂O₄ was observed in the XRD profiles, indicating that the solubility of Sr in Na layer was limited under 4 mol% (Figure S1b, Supporting Information). The scanning electron microscopy (SEM) images revealed hexagonal plate-shaped particles with an average size of 500 nm, regardless of the extent of Sr substitution (Figure S3, Supporting Information). Transmission electron microscopy (TEM) analysis was performed to gain further insights into the changes in crystal structure induced by Sr substitution. Specifically, high-angle annular dark field-scanning transmission electron microscopy (HAADF-STEM) analysis was conducted to certify the Sr substitution into the Na sites, and the obtained images directly validated the occupation of Na sites by Sr. O3-NCO and O3-NS4CO exhibited as hexagonal O3-type layered structure (Figure 1c,d). The enlarged atomic-resolution HAADF and annular bright field (ABF) images of the Na layers (right side of Figure 1c,d; related to the white-boxed region in Figure 1c,d) revealed a difference between O3-NCO and O3-NS4CO. The HAADF image of Na sites in O3-NCO was dark, owing to the small atomic number (*Z*) of Na,^[43] whereas that of O3-NS4CO certified the presence of high-*Z* Sr ions in the Na layer. The HAADF intensity profiles of O3-NS4CO showed small peaks corresponding to Sr in the Na layers, validating the substitution of Sr in the Na layers,

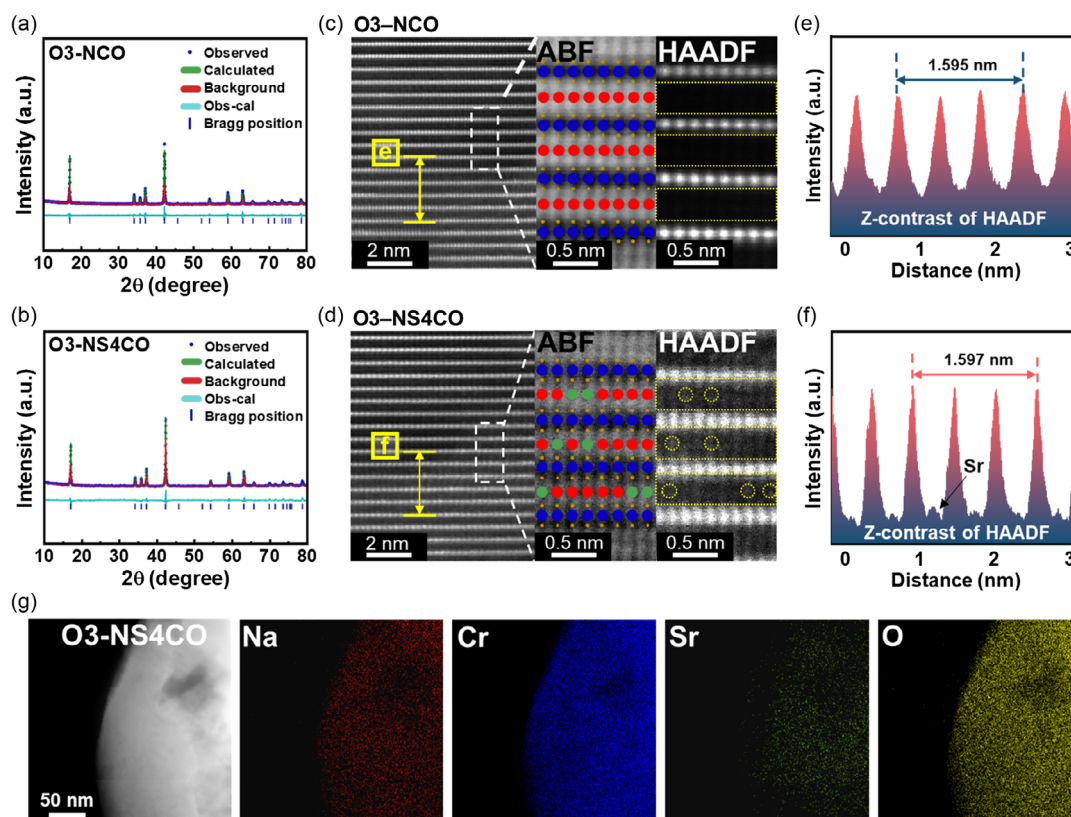


Figure 1. Rietveld-refined XRD patterns of a) O3-NaCrO₂ (O3-NCO) and b) O3Na_{0.92}Sr_{0.04}CrO₂ (O3-NS4CO). HAADF-STEM and ABF image of c) O3-NCO and d) O3-NS4CO. HADDF intensity profiles of e) O3-NCO and f) O3-NS4CO. g) TEM-EDX mapping images of O3-NS4CO.

whereas that of O3-NCO showed no peaks corresponding to the Na layers (Figure 1e,f). Furthermore, the lattice parameter *c* was measured as 15.95 and 15.97 Å for O3-NCO and O3-NS4CO, respectively, which corresponded to Rietveld refinement XRD results. The energy-dispersive X-ray spectroscopy (EDX) mapping results showed uniform distributions of elements for O3-NCO and O3-NS4CO (Figure 1g and S4, Supporting Information). These findings were corroborated by the density functional theory (DFT) results, which indicated that the Sr substitution into the Na sites exhibited a slightly more favorable site energy (−2.549 eV) than that corresponding to substitution into the Cr sites (−2.540 eV; Figure S5, Supporting Information). The small energy difference suggested a preference for Sr to substitute at the Na sites, aligning with the experimental observations from TEM analysis. Collectively, these findings enhance our understanding of the structural changes in O3-NS4CO due to Sr incorporation. Furthermore, we confirm the uniform substitution of Sr into O3-Na_{0.92}Sr_{0.04}CrO₂ cathode using TEM-EDX line scanning elemental analysis and DFT calculations (Figure S6, S7, Supporting Information).

2.2. Effects of Sr²⁺ Substitution into Na⁺ Sites on Electrochemical Performance

The O3-NCO cathode intrinsically experiences an irreversible phase transition after sodium extraction upon charging over a

voltage plateau at 3.8 V ($x > 0.5$ in Na_{1-x}CrO₂).^[32] To confirm the effects of Sr substitution on high-voltage stability, herein, the electrochemical properties of the O3-NCO, O3-NS2CO, O3-NS4CO, and O3-NS6CO cathodes were evaluated in the wide operating voltage range of 1.5–3.8 V (vs. Na/Na⁺). The galvanostatic first charge–discharge curves of the cathodes were acquired at a current rate of 0.1 C (Figure 2a, and S8a,b, Supporting Information). Although the high charge capacity of 204 mA g^{−1} was obtained in 1st charging up to 3.8 V, O3-NCO only delivered a very low discharge capacity of 81 mAh g^{−1} corresponding to low 1st coulombic efficiency (CE) of 39.7%. Upon the substitution of up to 4 mol% Sr, the reversible capacity and CE of the cathodes were gradually improved by reducing the plateau at 3.8 V. However, the reversible capacity of the O3-NS6CO cathode was relatively lower than that of O3-NS2CO and O3-NS4CO, evidently owing to the formation of electrochemically inactive SrCr₂O₄, as observed in the XRD patterns.^[43] Notably, the O3-NS4CO cathode exhibited the lowest hysteresis profile in the galvanostatic charge–discharge curve and results in the highest reversible capacity of 130 mAh g^{−1} with 1st CE of 91% compared to other samples. The noticeable differences in the reversible Na storage behavior between the samples at 1st cycle were reflected in the cycling test at a current rate of 1 and 10 C. For the cycling test at a current rate of 1 C (Figure S9, Supporting Information), the Sr-substituted cathodes demonstrated a higher reversible capacity than O3-NCO over 50 cycles; in particular, the O3-NS4CO cathode

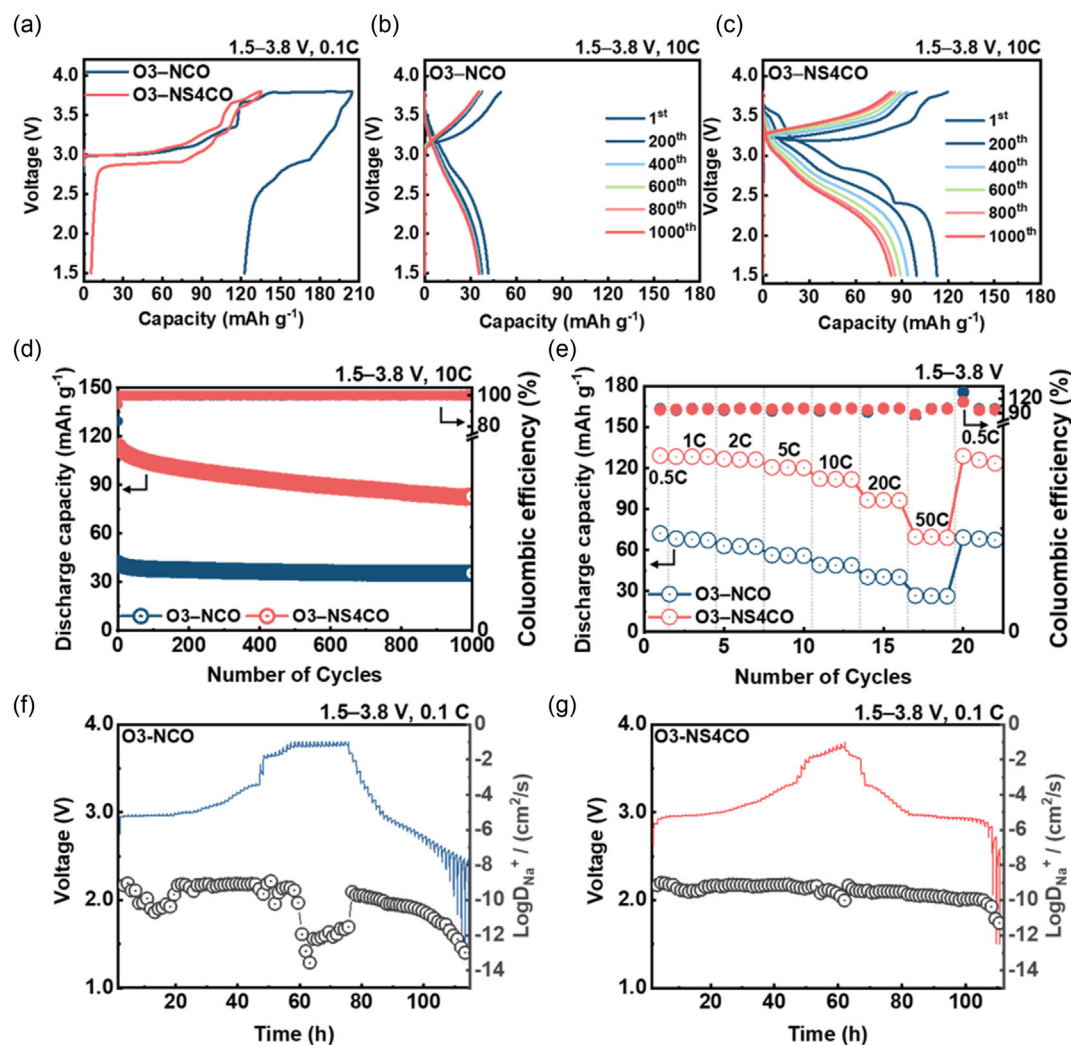


Figure 2. Electrochemical performance comparison of O3-NCO and O3-NS4CO: a) Initial charge–discharge curves at 0.1 C (1 C = 120 mA g^{−1}), selected charge–discharge curves of b) O3-NCO and c) O3-NS4CO, d) cycling performance at 10 C, and e) rate capability at current rates from 0.5 to 50 C in the voltage range of 1.5–3.8 V. Na⁺ diffusion coefficients of f) O3-NCO and g) O3-NS4CO calculated from GITT profiles.

delivered the highest reversible capacity of 105 mAh g^{−1} after 50th cycle. The differences in cycling stability and interfacial Na⁺ transfer kinetics were pronounced at a high current rate of 10 C (Figure 2b–d). O3-NCO showed poor Na⁺ storage capability with a remarkably low reversible capacity of 35 mAh g^{−1} over 1000 cycles. Surprisingly, O3-NS4CO exhibited a high discharge capacity of 85 mAh g^{−1} and demonstrated outstanding cycling stability with a capacity retention of 75% after 1000 cycles. The reversible capacity of O3-NS2CO and O3-NS6CO was significantly higher than that of O3-NCO but lower than that of O3-NS4CO (Figure S10, Supporting Information). At a various current rate ranging from 0.5 to 50 C, O3-NS4CO displayed superior power capability compared to other samples: specifically, O3-NS4CO delivered the highest reversible capacity of 70 mAh g^{−1} than O3-NCO (26 mAh g^{−1}), O3-NS2CO (62 mAh g^{−1}), and O3-NS6CO (46 mAh g^{−1}) (Figure 2e and S11, S12, Supporting Information). It should be noted that the presence of Ca²⁺ and Sr²⁺ in the Na layer can stabilize

the cycling stability by inhibiting the irreversible phase transition at high charging cut-off potentials; however, Sr–O bonds, which exhibited a relatively weaker net-effective charge than that of Ca–O bonds in the Na layers, could further improve the reversible capacity and high-power capability by facilitating Na⁺ diffusion kinetics while acting as a pillar (Figure S13, Supporting Information).^[34,40] Beyond the advantages of Ca substitution, Sr facilitates charge transfer reactions due to the electron delocalization characteristics.

To further investigate the impact of Sr substitution on Na⁺ diffusion kinetics, the diffusion coefficient of Na⁺ (D_{Na^+}) was determined using the galvanostatic intermittent titration technique (GITT) for O3-NCO and O3-NS4CO in the initial charge–discharge process at a current density of 12 mA g^{−1} with a 15 min pulse interval; the rest time was fixed at 1 h to reach a quasiaelectrochemical equilibrium voltage.^[44] Using the GITT data and Fick's second law of diffusion, the D_{Na^+} value for O3-NCO and O3-NS4CO was calculated using the equation^[45]

$$D_{\text{Na}^+} = \frac{4}{\pi \tau} \left(\frac{n_m V_m}{S} \right)^2 \left(\frac{\Delta E_s}{\Delta E_t} \right)^2 \quad (1)$$

where τ is the duration of the current pulse (s), n_m is the number of moles (mol), V_m is the molar volume ($\text{cm}^3 \text{mol}^{-1}$), S is the cathode area (cm^2), ΔE_s is the steady-state voltage difference due to the current pulse, and ΔE_t is the voltage change during the constant current pulse. The D_{Na^+} values calculated from the GITT curves as a function of the state of charge and discharge during the (de)sodiation (Figure 2f,g). Within the voltage window of 1.5–3.8 V, the D_{Na^+} value for O3-NS4CO was $3.13 \times 10^{-10} \text{ cm}^2 \text{s}^{-1}$, while O3-NCO showed a value of $5.51 \times 10^{-11} \text{ cm}^2 \text{s}^{-1}$, with notable fluctuation features. Notably, the D_{Na^+} value of O3-NCO at the end of the charge–discharge process was only one-fifteenth that of O3-NS4CO, indicating that the unfavorable irreversible phase transition in the high-voltage region led to sluggish Na-ion kinetics, which was effectively suppressed by Sr substitution. Consequently, the improved structural stability and the presence of generated Na^+ ions/vacancies facilitated sodium storage, resulting in excellent power capability.

To further investigate the electrochemical sodium storage behavior of O3-NCO and O3-NS4CO, multiscan rate cyclic voltammetry (CV) measurements were performed at rates ranging from 0.1 to 1 mV s^{-1} . As the scanning rate increased, similar CV patterns with enlarged and broadened peaks were obtained for O3-NCO and O3-NS4CO (Figure S14a,b, Supporting Information). Based on these results, the diffusion-controlled and capacitive capacity contributions of O3-NCO and O3-NS4CO calculated and compared using the following equation^[46]

$$i = av^b \quad (2)$$

where i represents the peak current (mA), v denotes the scan rate (mV s^{-1}), and a and b are fitting parameters. The calculated b values describe the storage process; if the value is 0.5, then it is exclusively a diffusion-controlled process; if the value is 1.0, it implies a capacity-controlled process. The value of b provides insight into the storage mechanism: a value of 0.5 indicates a fully diffusion-controlled process, while a value of 1.0 corresponds to capacitive process.^[47] By analyzing the $\log(i)$ versus $\log(v)$ relationship for different redox peaks, the calculated b -values for O3-NCO and O3-NS4CO were found to be 0.53 and 0.51, respectively, suggesting predominantly diffusion-controlled behavior for O3-NCO and O3-NS4CO (Figure S14c, Supporting Information). Furthermore, the relative contributions of diffusion- and capacitive-controlled processes to Na^+ storage were quantitatively determined using the following equation^[17]

$$i(V) = k_1 v + k_2 v^{1/2} \quad (3)$$

The first and second components correspond to the capacitive-controlled and diffusion-controlled redox reactions, respectively. Using this calculation, the capacitive and diffusion contributions were quantified for both cathodes. The overall diffusion contribution of O3-NS4CO was higher than those of O3-NCO at scan rates ranging from 0.1 to 1 mV s^{-1} (Figure S14d,e, Supporting Information). These results suggest that the reduced voltage polarization, achieved through enhanced structural stability

and faster Na ion kinetics through the Sr substitution strategy, contributes to improved electrochemical performances.

Electrochemical impedance spectroscopy (EIS) analysis was performed to examine the interfacial impedance and internal Na^+ diffusion coefficient for the O3-NCO and O3-NS4CO cathode after the 1st and 50th cycles at 1 C, respectively (Figure S15, Supporting Information).^[15,48] The Nyquist plot is fitted with an equivalent circuit as shown in Figure S15a, Supporting Information). The impedance spectrum was deconvoluted into the resistances associated with the bulk (R_b), the interfacial layer (R_{sei}), and charge transfer reaction (R_{ct}) (Table S3, Supporting Information). After the first cycle, O3-NS4CO exhibited a significantly lower R_{sei} and R_{ct} impedance than that of O3-NCO. The lower R_{sei} is attributed to the reduced irreversible phase transition accompanying electrolyte decomposition. The lower R_{ct} is attributed to the improved charge transfer kinetics resulting from the modified electronic structure by Sr substitution. Furthermore, O3-NS4CO showed a smaller impedance than that of O3-NCO after 50th cycle. These results confirmed that Sr substitution enhanced the structural stability and synergistically lower the electrode/electrolyte interface resistance,^[49] leading to improved Na ion kinetics.

2.3. Theoretical Studies

To evaluate the thermodynamic stability of the O3-NCO and O3-NS4CO compositions, the phase diagram at 0 K (also known as the convex hull) was computationally constructed for each ternary Na-(Sr)CO system. The calculations were based on the total energies of all elements, as well as binary and ternary compounds, which were determined using the DFT. Based on the energy calculation depicted in Figure 3a and S16a, Supporting Information, it can be observed that O3' and P'3 exhibits the lowest energy within the range of $1/4 < x < 2/3$ for O3-NCO and O3-NS4CO, indicating its superior stability compared to other phases. Upon extraction of all sodium ions ($x=0$), the O3 (O') phase became stable, with O3-NS4CO exhibiting a lower energy level than that of O3-NCO. The convex hull is formed by linking all the lowest formation energy states, using O3 at $x=1$ and O3 (O3') at $x=0$ as the reference states. This convex hull, represented by a dotted line in Figure 3a, is widely utilized as a direct indicator of thermodynamically stable phase at specific voltage region. The positions corresponding to $x=1/2$ and $2/3$, which were displayed on the convex hull, represented two additional stable intermediate phases. A comparison of the energy between O3-NS4CO and O3-NCO (Figure 3a and S16a, Supporting Information) suggested that Sr substitution led to a more stable lattice with a lower formation energy, indicating that the substituted phases were less likely to undergo unwanted phase transition, decomposition, or structural collapse during repeated charge–discharge cycles. This increase stability is primarily due to the strong cationic potential of Sr, which reduces lattice strain and strengthens the overall framework of the crystal structure, making it more resistant to the structural stress during the cycling. Figure 3b and S16b (Supporting Information) show the predicted redox potential range of the O3- Na_xCrO_2 and O3- $\text{Na}_x\text{Sr}_{0.04}\text{CrO}_2$ cathode as a function of the Na content $0.20 \leq x \leq 1$, $0.312 \leq x \leq 0.92$ overlaid with the charge and

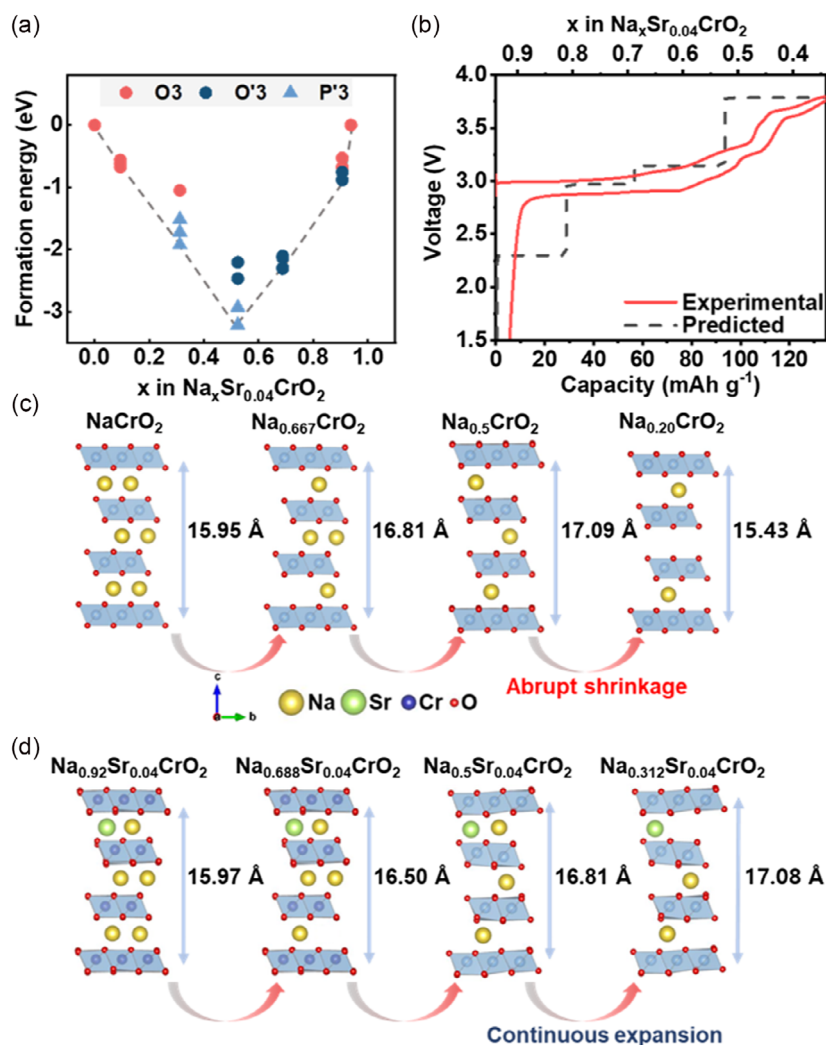


Figure 3. a) Convex hull plot of formation energy and b) theoretical redox potentials for O3-Na_xSr_{0.04}CrO₂ ($0.32 \leq x \leq 0.92$) predicted using first-principles calculations. Predicted structural changes of c) O3-NCO and d) O3-NS4CO during the charging.

discharge curves in the voltage range of 1.5–3.8 V. The theoretical capacity of O3-Na_{0.92}Sr_{0.04}CrO₂ in the voltage range of 1.5–3.8 V was $\approx 132 \text{ mAh g}^{-1}$, considering the Cr³⁺/Cr⁴⁺ redox reaction associated with 0.6 mol of Na ions. Three major intermediate phases were observed at 1.5 and 3.8 V upon charging, which corresponded to the Na content of 1/2 and 1/3, respectively. In summary, as revealed by the electrochemical results and the computational data, we can conclude that reversible Na⁺ (de) insertion can be achieved in O3-Na_xSr_{0.04}CrO₂ cathode for Na content $0.312 \leq x \leq 0.92$ within the 1.5–3.8 V voltage range. To obtain further insight into the phase transition during the charge process, the crystal structure changes in O3-Na_xCrO₂ and O3-Na_xSr_{0.04}CrO₂ as a function of the Na content $0.20 \leq x \leq 1$, $0.312 \leq x \leq 0.92$ were analyzed. The change in phase and c-axis during desodiation have been described in Figure 3c,d for O3-Na_xCrO₂ and O3-Na_xSr_{0.04}CrO₂. In the initial stages of desodiation (from NaCrO₂ to Na_{0.5}CrO₂), the removal of sodium ions led to expansion along the c-axis. After Na_{0.5}CrO₂ was produced, further desodiation (from Na_{0.5}CrO₂ to

Na_{0.20}CrO₂) led to compression along the c-axis. This could be due to the reduction in electrostatic repulsion within the layers of the structure as sodium ions are removed and more significant structural rearrangement or phase transition that occurs at this stage of desodiation,^[30,31] which enables the sodium-ion diffusion barrier to be reduced greatly. However, in terms of the overall desodiation, O3-Na_xSr_{0.04}CrO₂ demonstrated continuous c-axis expansion without any abrupt shrinkage, owing to the presence of electrochemically inactive Sr²⁺ and strong Sr–O bonds that enhanced the structural stability in the highly charged state.

The theoretical pathways and required energies for Cr migration to the Na layer were compared between O3-Na_{0.20}CrO₂ and O3-Na_{0.312}Sr_{0.04}CrO₂ (Figure 4a,b). In the O3-Na_{0.20}CrO₂ case, the thermodynamic energy of tetrahedral and octahedral sites in alkali metal sites is lower than that of octahedral sites in transition metal. Upon charging to potentials over 3.8 V, Cr ions could migrate from octahedral sites within the CrO₂ slab to tetrahedral sites in the interslab space and subsequently to

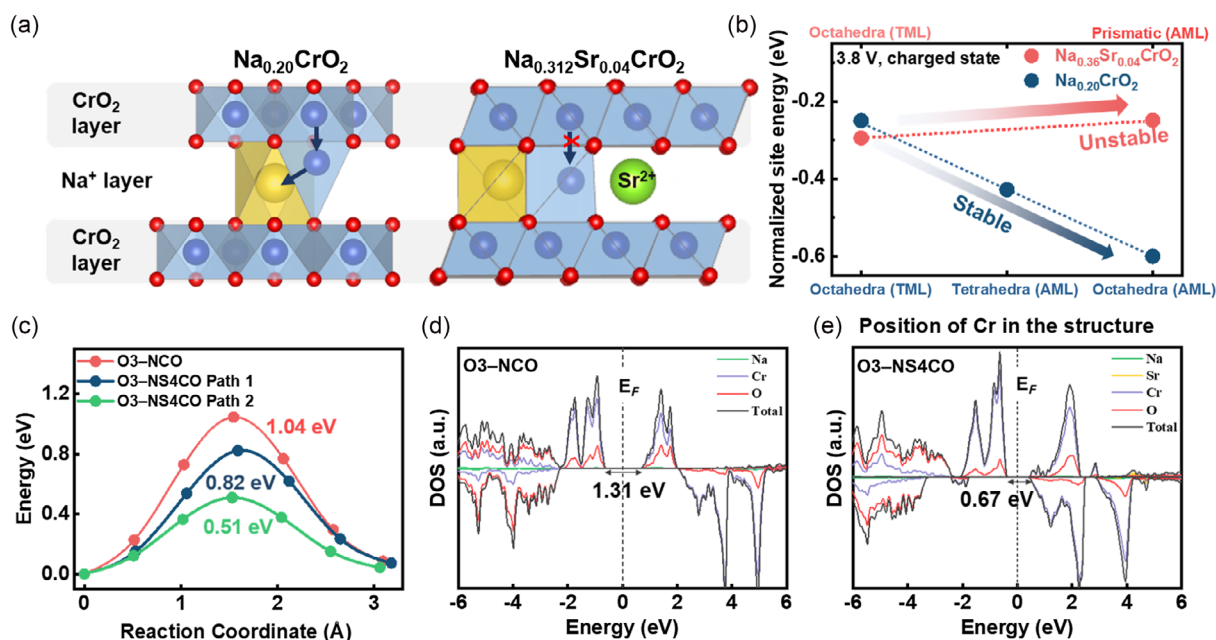


Figure 4. a) Crystal structures of tetragonal and octahedral sites where Cr ions can migrate in Na_{0.20}CrO₂ (left) and Na_{0.36}Sr_{0.04}CrO₂ (right). b) Comparison of the formation energy as a function of the position of Cr-ion in Na_{0.20}CrO₂ and Na_{0.36}Sr_{0.04}CrO₂. c) Predicted activation barrier energy for Na⁺ ion diffusion. Calculated total density of state for d) O3-NCO and e) O3-NS4CO.

octahedral sites that were face-shared with the tetrahedral sites. However, P3-type Na_{0.312}Sr_{0.04}CrO₂ case, the prismatic site in the alkali metal layer has a higher value than the octahedral site in the CrO₂ slab. These results indicated that the Sr substitution in the Na site was thermodynamically challenging to migrate to the octahedral site in the CrO₂ slab. Because a strong Sr–O bond enhances the overall structural stability and electrochemically inactive Sr ion plays a role as a pillar; we speculate that the enhanced structure reversibility during the charge and discharge at the voltage range of 1.5–3.8 V. To confirm the superior rate capability of the O3-NS4CO than O3-NCO, we conducted nudged elastic band (NEB) calculation and projected density of state (PDOS) (Figure 4c–e). Figure 4c depicts the diffusion barrier and energy profile along the diffusion channel for Na in O3-NCO, O3-NS4CO (path 1: remote from Sr ion), and O3-NS4CO (path 2: nearby Sr ion). Figure S17, Supporting Information, describes the ion migration pathways for all the cases. The Sr substituted cathode shows a relatively lower energy barrier compared to O3-NCO regardless of diffusion path. The diffusion barrier for sodium ions is particularly low, measuring roughly 0.51 eV for migration near Sr ion while 0.82 eV for far from Sr ion in O3-NS4CO. In comparison, O3-NCO shows a high value (1.02 eV) of diffusion barrier (Figure 4c). Sr-substituted O3-NCO showed a relatively low diffusion barrier owing to the roles of the Sr-substitution-induced Na⁺/vacancies in enhancing the Na⁺ mobility within the structure. Moreover, the Na⁺ diffusion path near the Sr ion exhibited the lowest diffusion barrier. Because Sr ions have a positive charge, the probability that a vacancy exists nearby is relatively greater than the probability that a Na ion exists, resulting in higher Na⁺ diffusivity than all the structures. O3-NS4CO (near Sr ion), which was used as an electrode material for SIBs, demonstrated excellent rate

performance. The total density of states (TDOS) was calculated to further explore the electronic structure of O3-NCO and O3-NS4CO (Figure 4d,e). In density of states (DOS), it is shown that the O3-NCO and O3-NS4CO material exhibits metallic features, which endows O3-it with a fast charge and discharge rate. The substitution of Sr for Na was also expected to alter the electronic properties of the cathode and thereby improve the overall electrochemical behavior through enhanced charge transfer kinetics. According to the DOS near the Fermi level, O3-NCO and O3-NS4CO exhibited ferromagnetism before desodiation in TDOS, mainly contributed by the Cr-d orbital electrons in PDOS. Additionally, the O3-NS4CO structure is induced by strong charge transfer, which enables the sodium-ion diffusion barrier to be significantly reduced. Overall, the DOS and NEB calculations affirmed the beneficial effects of Sr substitution on enhancing the Na-ion diffusion kinetics and the electronic conductivity of O3-NS4CO.

2.4. Analysis of the Structural Evolution via Synchrotron-Based X-ray Techniques

To understand the structural evolution induced by Sr substitution into the Na layer, in situ XRD analysis was conducted during the first charge–discharge process of the cathodes. A series of XRD patterns was collected at different states of charge within the voltage range of 1.5–3.8 V (vs. Na/Na⁺), and the corresponding intensities were displayed in a contour plot with specified scanning angle (2θ) domains of 15–18°, 31–38°, 40–43°, 43–47°, and 60–65° (Figure 5a,b). Additionally, the corresponding variations in lattice parameters were studied (Figure 5a,b). Similar to those of O3-NCO, the peaks representing the (003)

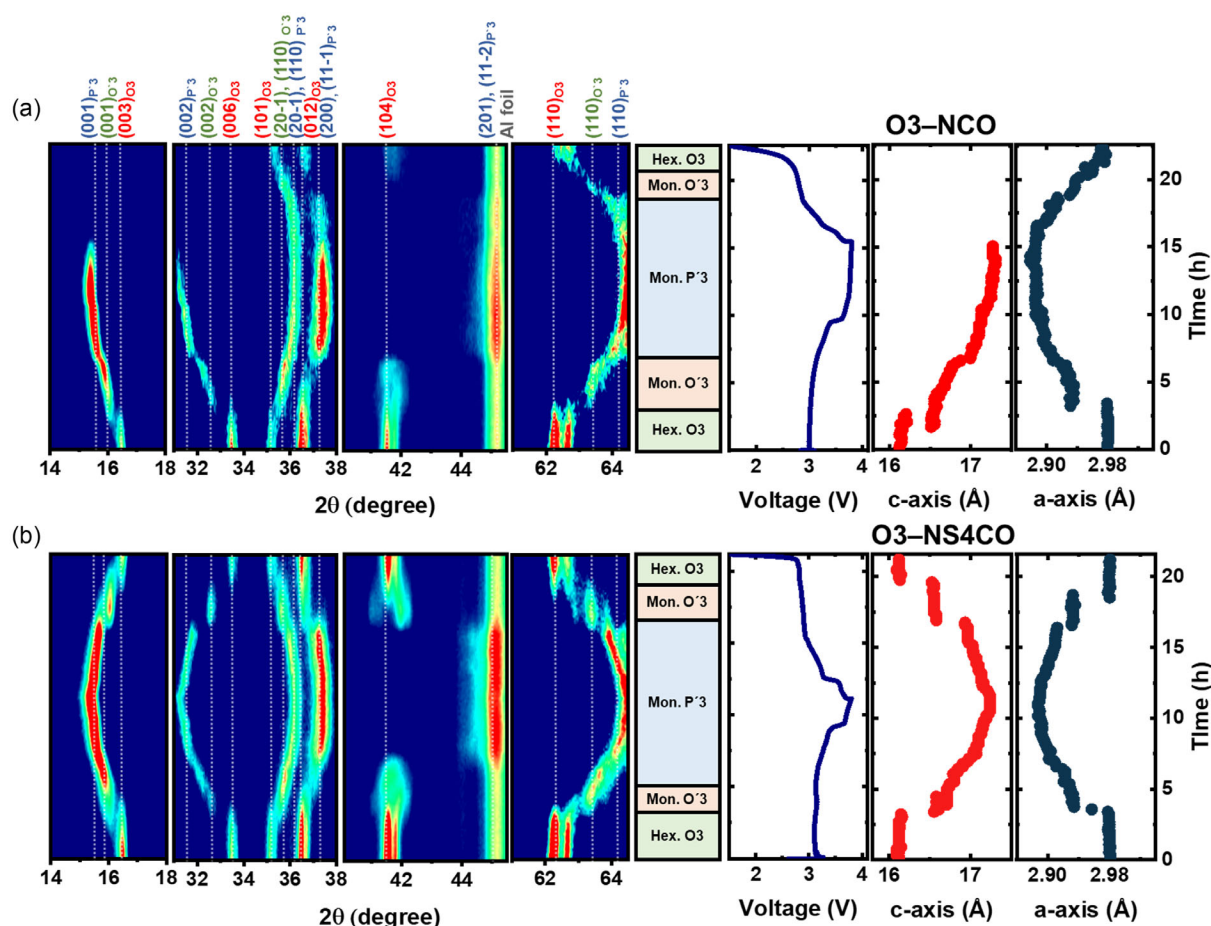


Figure 5. Contour plots, charge–discharge curve, and lattice parameters of *b*-axis and *c*-axis during the first charge and discharge at 0.1 C, obtained via in situ XRD measurements, for a) O3-NCO and b) O3-NS4CO in the voltage range of 1.5–3.8 V.

and (006) crystal faces of O3-NS4CO shifted toward lower diffraction angles, whereas those corresponding to the (101), (012), and (110) planes moved to higher scanning angles. These results indicated an evolution from the hexagonal O3 (O₃_{hex}) phase to the monoclinic P'3 (P'3_{mon}) phase via the monoclinic O'3 (O'3_{mon}) phase through the gliding of CrO₂ slabs accompanied by extraction of Na ions. In the early stage of desodiation at 3.03 V, the characteristic peaks of the O3_{hex} phase, such as (003) and (104), shifted and/or split into two peaks, confirming the formation of O'3_{mon} phase. During the subsequent charging to 3.8 V, the peaks related to both O3_{hex} and O'3_{mon} phases gradually disappeared, accompanied by the transition to P'3_{mon} phase. Consequently, the phase transformations and their orderly sequence were reversible as the original O3_{hex} phase was completely recovered during subsequent discharging. This extraction of Na ions induced the typical O3_{hex}–O'3_{mon}–P'3_{mon} phase transition through the gliding of CrO₂ slabs.^[30] The O3-NS4CO electrode permitted reversible electrochemical reactions, leading to continuous phase transitions, thereby enabling complete recovery to the original state upon discharge. In contrast, O3-NCO exhibited discontinuous phase transitions. Upon charging to 3.8 V, the (003) and (006) peaks shifted toward lower angles and decreased in intensity, but did not recover upon

discharging. The irreversibility of the (003) and (006) peaks resulted from Cr migration, during which Cr ions moved from octahedral sites in the TM layer to tetrahedral sites in the Na layer, causing lattice contraction along the *c*-axis.^[31,50] Additionally, the lattice parameters corresponding to the *c*-axis and *b*-axis were calculated. The increase in the *c*-axis lattice parameter during charging was attributed to the extraction of Na ions, which induced a repulsive force between O^{2–} ions, whereas the decrease in the *b*-axis lattice parameter was related to the reduction in ionic radius caused by the oxidation of Cr ions.^[31,51] The changes in lattice parameters for the *b*-axis and *c*-axis confirm that O3-NS4CO undergoes smaller values compared to O3-NCO. The improved structural stability originated from the introduction of electrochemically inactive Sr ions as pillars, which suppressed the expansion of the *c*-axis lattice and inhibited Cr migration to the Na layer during charging. Therefore, the O3-NS4CO electrode exhibited robust structural stability at an ultrahigh voltage of 3.8 V (vs. Na/Na⁺), contributing to reversible phase transitions and enabling high specific capacity.

X-ray absorption near-edge structure (XANES) analysis was conducted to gain insights into the charge compensation mechanism of O3-NCO and O3-NS4CO. Reference spectra of Cr₂O₃

(Cr³⁺) and CrO₃ (Cr⁶⁺) were used to identify the valence state of chromium.^[52] The Cr K-edge spectra revealed that the average oxidation state of Cr in pristine O3-NCO and O3-NS4CO was 3+, indicating that no visible differences were observed between the two samples in terms of oxidation state (Figure 6a). This result confirms that O3-NCO and O3-NS4CO samples were well synthesized with respect to stoichiometry. After charging to 3.8 V, the pre-edge peak (5992 eV) shifted to higher energy (5994 eV), indicating the oxidation state of chromium ions changed from 3+ to 4+ owing to the extraction of Na ions. In O3-NCO, the Cr⁴⁺ ions in the TM layer underwent a disproportionation reaction when more than 0.5 mol of Na ions were extracted from the structure in the high-voltage region. Because the CrO₂ slab mainly comprised Cr⁴⁺ ions in the high-voltage region, unstable Cr⁴⁺ (3d₂) readily transformed into stable Cr³⁺ (3d₃) and Cr⁶⁺ (3d₀) via disproportionation, as follows^[30,48]



The intensity of the peak at 5994 eV was higher for O3-NCO than for O3-NS4CO (Figure 6b), signifying an increase in the amount of Cr⁶⁺ in O3-NCO. This confirmed that O3-NS4CO did not exhibit the plateaus at ≈3.8 V (Figure 2a), suggesting that strong Sr–O bonds and inactive Sr increased the high-voltage structural stability and suppressed the unfavorable phase transition with respect to Cr⁶⁺ migration. After discharging at 1.5 V, significant differences were observed between the pre-edge peaks of the two samples. O3-NS4CO showed reversible recovery of the

Cr³⁺ oxidation state, whereas O3-NCO exhibited irreversible properties with a residual Cr⁶⁺ content (Figure 6c), indicating that O3-NS4CO underwent a reversible phase transition while O3-NCO did not, which is consistent with the in situ XRD results. Furthermore, we investigated the local charge environments of O3-NCO and O3-NS4CO during the charge/discharge process using extended X-ray absorption fine structure spectroscopy (EXAFS). The two intense peaks at the Cr–K-edge in the 1–3 Å range were associated with Cr–O coordination and a Cr–Cr second coordination.^[53] To determine the reversibility of the O3-NCO and O3-NS4CO electrodes in the pristine, charged, and discharged states, changes in the local structure of the Cr–O and Cr–Cr bonds were examined. As shown in Figure 6d, the peak intensity of the Cr–O and Cr–Cr bond length decreased and shifted slightly lower distance due to the extraction of Na ion from the structure.^[53] After discharging at 1.5 V, the peak position and intensity remained almost identical to that of the charged state because the disproportionation reaction product of Cr ion migrated to octahedral sites in the Na layers during charging. The Cr ions octahedrally trapped in the Na layers no longer participated in the Cr redox reactions, which led to a decrease in reversible capacity. In contrast, the Cr–O and Cr–Cr bonds recovered reversibly during discharging because the Sr in the Na layers effectively suppressed Cr migration in the highly charged state (Figure 6d,e). In situ XRD, XANES, and EXAFS studies verified that Sr substitution into the Na layers relieved structural stress and enhanced reversibility during the charge–discharge process. The introduction of inactive Sr ions

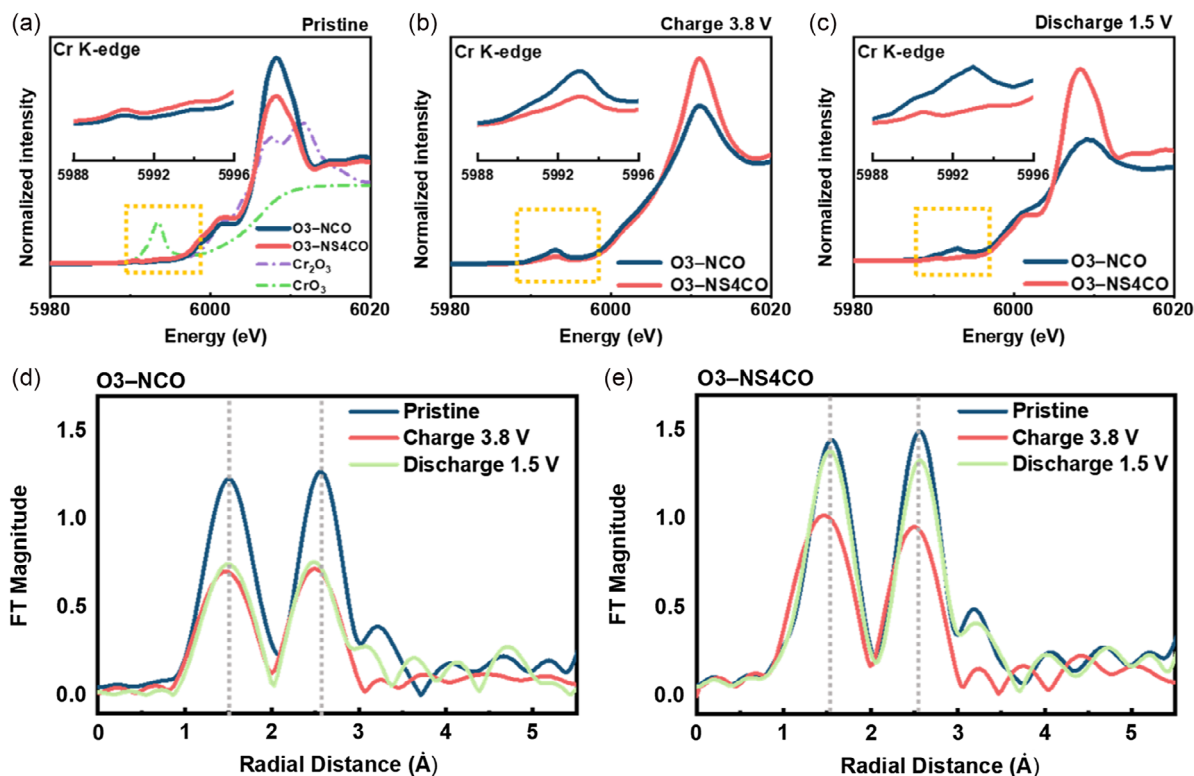


Figure 6. Ex situ XANES spectra at the Cr-K edge for O3-NCO and O3-NS4CO in a) pristine, b) charged, and c) discharged states. Corresponding ex situ EXAFS spectra at the Cr-K edge for d) O3-NCO and e) O3-NS4CO electrodes during charging and discharging.

into the Na layers enhanced the TM–O bond strength, thereby significantly improving the high-voltage stability of the O3-type structure. Consequently, the irreversible phase transition and Cr ion migration were considerably hindered during electrochemical processes, while improving long-term cycling.

2.5. Practical Applicability

To evaluate the practical applicability of the cathodes, we assembled pouch-type full cells using O3-NCO and O3-NS4CO as the cathode, and HC as the anode, photographically represented in Figure 7a. For practical considerations, the HC anode was used without pre-sodiation. The assembled pouch-type full cells were subjected to galvanostatic charge–discharge testing at current rates of 0.1, 0.2, and 0.5 C after degassing during the first cycle in the voltage range of 1.0–3.7 V. After degassing, the initial specific capacity of the O3-NCO//HC and O3-NS4CO//HC systems at 0.1 C was 100 and 101 mAh g^{−1}, respectively, with the corresponding CEs being 95% and 96.9% (Figure 7b,c). The HC used as the anode for the full cell exhibited almost 100% CE and stable cyclability (Figure S18, Supporting Information), implying that the full-cell capacity fading during cycling was mainly attributed to cathode performance degradation rather than that of the HC anode. Following 250 cycles, the capacity retention for the pouch full cell with O3-NS4CO was 62.6% with Coulombic efficiency remaining close to 100%, whereas for the one with O3-NCO remained only 34.4% (Figure 7d, and S19a, S19b, Supporting Information). The CE of O3-NCO fluctuated between 97% and 104% after 30 cycles, indicating the potential instability of the crystal structure and electrode–electrolyte interface.

X-ray photoelectron spectroscopy (XPS) analysis was conducted to examine the differences in electrochemical performance upon cycling. The Cr 2p XPS profiles of the cycled O3-

NCO and O3-NS4CO cathodes highlighted the difference in the oxidation state of Cr ions (Figure 7e,f). The cycled O3-NCO electrode exhibited a larger fraction of Cr⁴⁺ ions than that of the cycled O3-NS4CO electrode, indicating a delayed disproportionation reaction in O3-NS4CO (Figure 7g). The low presence of Cr⁴⁺ after cycling for O3-NS4CO indicated that Sr substitution in Na layer enhanced structural stability, which led to a significant increase in reversibility. Additionally, XPS analysis was performed on the surface of HC in the pouch-type full cells to explore the surface chemistry of the anode side (Figure S20, S21, Supporting Information). The P 2p and F 1s XPS profiles indicated the decomposition of the electrolyte salt during cycling. The P 2p XPS spectrum revealed less formation of Na_xPO_yF_z in the HC anode cycled with the O3-NS4CO cathode than HC anode cycled with the O3-NCO cathode. Similarly, the F 1s spectrum indicated reduced formation of NaF in the HC anode cycled with the O3-NS4CO cathode. The formation of Na_xPO_yF_z and NaF on the surface of the anode was associated with electrolyte decomposition; therefore, the restricted formation of these chemical species in the pouch-type full cell assembled with the O3-NS4CO cathode indicated inhibition of the irreversible transitions induced by electrolyte decomposition.^[53] In contrast, in the pouch-type full cell with the O3-NCO cathode, the formation of a thick solid electrolyte interphase (SEI) layer on the anode surface owing to electrolyte decomposition presumably resulted in the low reversibility of the anode and the fluctuation in CE.

Not only the electrochemical performance of the cathode for SIBs, but the thermal stability of cathode materials is also an important factor limiting the commercial application of SIBs. Therefore, the thermal stability of the O3-NCO and O3-NS4CO electrodes (charged to 3.8 V) was investigated by conducting differential scanning calorimetry (DSC) at a heating rate of 5 °C min^{−1} (Figure 7h). The onset temperature of thermal decomposition for

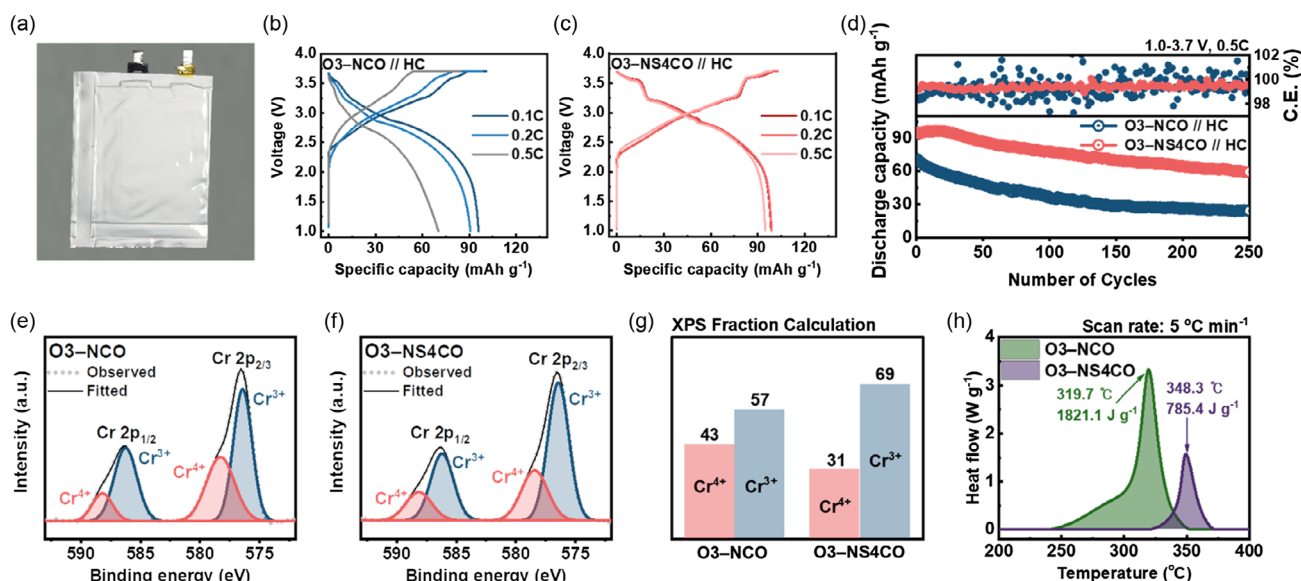


Figure 7. a) The photograph of the pouch-type full cell. Charge–discharge curves of pouch-type full cell with b) O3-NCO and c) O3-NS4CO cathodes with HC anode at different current rates (0.1–0.5 C) in the voltage range of 1.0–3.7 V. d) Cycling performance of full cells at 0.5 C. Ex-situ Cr 2p XPS profiles of e) O3-NCO and f) O3-NS4CO after 250 cycles, g) atomic contents of Cr³⁺ and Cr⁴⁺ in O3-NCO and O3-NS4CO, obtained from Cr 2p XPS profiles. h) DSC results of charged O3-NCO and O3-NS4CO.

charged O3-NCO and O3-NS4CO electrodes was 319.7 and 348.3 °C, respectively. Additionally, the exothermic heat generation for O3-NS4CO (785.4 J g⁻¹) was lower than that for O3-NCO (1821.1 J g⁻¹). This result indicated that O3-NS4CO exhibited superior thermal stability, presumably owing to the strong Sr–O bonds in its crystal structure.^[54–56] In other words, Sr substitution enhanced the structural stability, leading to reduced oxygen evolution within the lattice and reducing thermal damage.

3. Conclusion

In summary, for the first time, we proposed a Sr substitution into the Na site, which significantly enhances the structural stability and electrochemical properties of the O3-NCO cathode. Upon using optimal Sr substitution level of 4 mol%, the O3-NS4CO cathode delivered a high initial specific capacity of 130 mAh g⁻¹ with an improved long-term cycling stability of 75% after 1000 cycles at a current rate of 10 C and significantly high-power capability with a specific capacity of 53% at 50 C (vs. 0.1 C). GITT and EIS analysis results showed that the enhanced power capability was associated with the significantly enhanced Na⁺ kinetics due to the Na⁺ ions/vacancies created by Sr substitution. A combination study of XANES, EXAFS, and in situ XRD analyses verified that the improved structural stability, which emanated from the strong Sr–O bonds, reinforced the phase reversibility and, thereby, cyclability of O3-NS4CO. Moreover, the O3-NS4CO cathode demonstrated good practical applicability with high thermal stability and long-term cycling stability in the pouch-type full cell using hard carbon anode. Theoretical studies precisely confirmed that the outstanding electrochemical performance could be ascribed to the high structural stability and rapid Na-ion kinetics resulting from Sr substitution into the Na layers. We believe that the proposed Sr substitution strategy will provide new inspiration for the development of practical cathode materials for high-energy density SIBs.

4. Experimental Section

Material Synthesis: The O3-Na_{1-2x}Sr_xCrO₂ samples ($x = 0, 0.02, 0.04$, and 0.06) were synthesized through a simple solid-state reaction. Starting materials included stoichiometric sodium carbonate (Na₂CO₃; 99%, Aldrich), strontium oxide (SrO; 99.9% Aldrich), and chromium oxide (Cr₂O₃; 98% Aldrich). The precursor powders were thoroughly mixed, pulverized, and then annealed at 900 °C for 10 h in a tube furnace under an argon atmosphere. After natural cooling to room temperature, the sample was removed and stored in an argon-filled glove box.

Electrochemical Measurements: The working electrode for the electrochemical tests was prepared by combining the active materials (80 wt%), Super P (5 wt%), KS-6 (5 wt%), and N-methyl pyrrolidone (NMP) (10 wt%). The resulting slurry was then uniformly deposited onto a carbon-coated Al foil, which served as the current collector, and then dried overnight under vacuum at 80 °C. The dried foil was hot-pressed at 120 °C between stainless-steel twin rollers for uniformity and punched into circular discs (ϕ14 mm). The average loading weight of the active materials on the dried electrodes was ≈3 mg cm⁻². A CR 2032-type coin cell was assembled using the fabricated cathode, Na metal as the counter electrode, and 1 M NaPF₆ in ethylene carbonate/diethylene carbonate (EC/DEC; 1:1 mixture by volume) with 5 wt% fluoroethylene carbonate (FEC). The same amount of electrolyte (100 μL) was injected into each cathode material. Galvanostatic charge–discharge tests and EIS were performed at various current densities in the voltage range of 1.5–3.8 V (vs. Na/Na⁺;

1 C = 120 mA g⁻¹) using a programmable battery tester (TOSCAT) and a Bio-Logic Science Instruments device, respectively. To assess the practical viability of the designed cathode, pouch-type (3 × 5 cm) full cells were fabricated and tested in the voltage range of 1.0–3.7 V (vs. Na/Na⁺). HC was used as the anode in these experiments. To that end, a homogeneous slurry formed by blending HC (80 wt%) and polyvinylidene fluoride (20 wt%) was coated on a Cu foil and vacuum dried at 110 °C for 12 h. Additionally, the N/P (anode/cathode) ratio was maintained at 1.2:1 while constructing the full cell.

Material Characterization: The element composition of the samples was estimated by ICP-OES using a PerkinElmer 4300 DV analyzer. The crystal structure and morphology of the prepared powders were identified by XRD using a diffractometer with Cu K_α radiation ($\lambda = 1.54178 \text{ \AA}$) over a 2θ range of 10–80°. The raw XRD data of all samples were refined using the Rietveld process with GSAS-II software, and the structural models derived from the refined data were constructed using VESTA. The microstructure of each sample was examined by field-emission scanning electron microscopy (FE-SEM) and high-resolution transmission electron microscopy, whereas elemental mapping was conducted by EDX using JSM-7900F and SU5000 systems. TEM and STEM were performed using an aberration-corrected JEM-ARM200F device operated at 200 kV. HAADF-STEM and ABF images were acquired using collection semiangles of 54–220 mrad and 11–22 mrad, respectively, with a convergence semi-angle of 21 mrad. EDX mapping was performed in STEM mode. Synchrotron-based operando analysis for in situ XRD variations on the cathode was conducted at the Pohang Accelerator Laboratory (PAL) using the 1D XRD KIST-PAL beamline. A MAR345 image plate detector was employed, operating at the synchrotron source with an energy of 2.5 GeV and a maximum storage current of 200 mA. The X-ray beam was focused with a toroidal mirror and monochromatized to 12. The beam is focused vertically and horizontally, and high-resolution monochromatic X-rays are provided using a silicon (111) plane. The patterns were initially recorded at a wavelength of 0.999 Å, but the XRD patterns were subsequently plotted after recalculating the 2θ values using the conventional Cu K_α radiation (1.5414 Å). To conduct ex situ measurements on all the recovered samples in the pristine, charged, and discharged states, synchrotron XAS was conducted using the BL7D beamline at the high-energy 2.5 GeV Pohang Light Source (PLS) at a current of ≈200 mA. The collected data were converted using ATHENA software. The components of the cathode and anode surfaces after cycling were investigated by XPS: PHI 5000 VersaProbe.

Computational Details: The Vienna Ab initio Simulation Package^[57] was used with the DFT for geometry optimization and computing the electronic properties of the O3 phase of NaCrO₂ and Na_{0.92}Sr_{0.08}CrO₂. Interactions between valence electrons and ions were modeled using pseudopotentials based on the projector augmented wave (PAW) method. The Perdew–Burke–Ernzerhof (PBE) functional, a generalized gradient approximation (GGA), was employed to describe the exchange–correlation of valence electrons.^[58] To address the localization of d-orbitals in Cr, the GGA + U approach was adopted, with the U value set at 3.5 eV. Optimization simulations were performed using the conjugate gradient method, with the force tolerance maintained at 0.01 eV Å⁻¹. The kinetic energy cutoff was set at 430 eV, and Gamma k-point sampling grids of $10 \times 10 \times 2$ and $8 \times 8 \times 2$ were employed for supercells of (2 × 2) O3-type NaCrO₂ and (4 × 4) O3-type Na_{0.92}Sr_{0.08}CrO₂. All calculations incorporated spin polarization, initialized with a high-spin configuration, and the Grimme-d3 functional was used along with external ion incorporation. Previously reported methods were adopted to compute formation energy, convex hull, and voltage.^[59] To theoretically confirm the possibility of Cr migration in O3-NCO and O3-NS4CO, calculations were performed to compare the phase stability by targeting Frenkel-like defect formation energies at 3.8 V. Specifically, scenarios in which interstitial Cr ions occupy tetrahedral or octahedral vacancies in the interlayer layer were targeted, which represented the Cr migration model. A low E_{mig} value indicated a greater propensity for Cr to migrate, and this assessment was performed using the equation^[60]

$$E_{\text{mig}} = E_{\text{Cr-migrated}} - E_{\text{Pristine}} \quad (5)$$

Supporting Information

Supporting Information is available from the Wiley Online Library or from the author.

Acknowledgements

This research was supported by the National R&D Program through the National Research Foundation of Korea (NRF), funded by the Ministry of Science and ICT (RS-2024-00408156) of the Republic of Korea. This research was also supported by the Nano & Materials Technology Development Program through the National Research Foundation of Korea (NRF) funded by the Ministry of Science and ICT (RS-2024-00449682).

Conflict of Interest

The authors declare no conflict of interest.

Author Contributions

Gwangeon Oh: conceptualization (lead); formal analysis (equal); writing—original draft (equal). **Yunjae Oh:** data curation (equal); formal analysis (equal); writing—original draft (equal). **Shivam Kansara:** formal analysis (equal); investigation (equal); software (lead). **Heesung Shin:** formal analysis (equal); investigation (supporting); methodology (supporting). **Hyokyong Kang:** formal analysis (equal); investigation (supporting); methodology (supporting). **Tae-Hoon Kim:** formal analysis (equal); visualization (equal). **Dominic Bresser:** supervision (equal); validation (equal); visualization (equal). **Jang-Yeon Hwang:** supervision (equal); validation (equal); writing—original draft (lead); writing—review and editing (lead). **Gwangeon Oh, Yunjae Oh, and Shivam Kansara** contributed equally to this work.

Data Availability Statement

The data that support the findings of this study are available from the corresponding author upon reasonable request.

Keywords

high energies, high voltage, layered cathodes, sodium-ion batteries, substitution

Received: October 22, 2024

Revised: December 6, 2024

Published online:

- [1] A. Konarov, S.-T. Myung, Y.-K. Sun, *ACS Energy Lett.* **2017**, 2, 703.
- [2] B. Scrosati, J. Hassoun, Y.-K. Sun, *Environ. Sci.* **2011**, 4, 3287.
- [3] D. M. Davies, M. G. Verde, O. Mnyshenko, Y. R. Chen, R. Rajeev, Y. S. Meng, G. Elliott, *Nat. Energy* **2019**, 4, 42.
- [4] J. Xie, Y.-C. Lu, *Nat. Commun.* **2020**, 11, 2499.
- [5] T. Kim, W. Song, D.-Y. Son, L. K. Ono, Y. Qi, *J. Mater. Chem. A* **2019**, 7, 2942.
- [6] F. Degen, *J. Ind. Ecol.* **2023**, 27, 964.
- [7] J. M. Tarascon, *Joule* **2020**, 4, 1616.
- [8] J.-Y. Hwang, S.-T. Myung, Y.-K. Sun, *Chem. Soc. Rev.* **2017**, 46, 3529.
- [9] N. Yabuuchi, K. Kubota, M. Dahbi, S. Komaba, *Chem. Rev.* **2014**, 114, 11636.
- [10] N. Ortiz-Vitoriano, N. E. Drewett, E. Gonzalo, T. Rojo, *Energy Environ. Sci.* **2017**, 10, 1051.
- [11] X. Liang, J.-Y. Hwang, Y.-K. Sun, *Adv. Energy Mater.* **2023**, 13, 2301975.
- [12] X. Xia, J. R. Dahn, *J. Electrochem. Soc.* **2015**, 159, A1048.
- [13] J.-Y. Hwang, S.-T. Myung, D. Aurbach, Y.-K. Sun, *J. Power Sources* **2016**, 325, 106.
- [14] J.-Y. Hwang, C. S. Yoon, I. Belharouak, Y.-K. Sun, *J. Mater. Chem. A* **2016**, 4, 17952.
- [15] J.-Y. Hwang, T.-Y. Yu, Y.-K. Sun, *J. Mater. Chem. A* **2018**, 6, 16854.
- [16] J. Lee, J. Baek, Y. Kim, W. Jeong, H. Kim, G. Oh, Y. Oh, S. Jeong, S. Kansara, B. Sambandam, J.-Y. Hwang, J. Kim, *Mater. Today Chem.* **2023**, 33, 101741.
- [17] J. Lee, S. Park, Y. Park, J. Song, B. Sambandam, V. Mathew, J.-Y. Hwang, J. Kim, *Chem. Eng. J.* **2021**, 422, 130052.
- [18] S. Park, W. Park, V. Soundharrajan, V. Mathew, J.-Y. Hwang, J. Kim, *Chem. Eng. J.* **2021**, 404, 126974.
- [19] X.-X. Zhao, X.-T. Wang, Z.-Y. Gu, J.-Z. Guo, J.-M. Cao, Y. Liu, J. Li, Z.-X. Huang, J.-P. Zhang, X.-L. Wu, *Adv. Funct. Mater.* **2024**, 34, 2402447.
- [20] Q.-M. Yin, Z.-Y. Gu, Y. Liu, H.-Y. Lu, Y.-Y. Liu, Y.-N. Liu, M.-Y. Su, J.-Z. Guo, X.-L. Wu, *Adv. Funct. Mater.* **2023**, 33, 230406.
- [21] L. Wen, J. Zhang, J. Zhang, L. Zhao, X. Wang, S. Wang, W. Li, J. Luo, J. Ge, W. Chen, *eScience* **2024**, 100313, <https://doi.org/10.1016/j.esci.2024.100313>.
- [22] J. Zhang, Y. Yan, X. Wang, Y. Cui, Z. Zhang, S. Wang, Z. Xie, P. Yam, W. Chen, *Nat. Commun.* **2023**, 14, 3701.
- [23] C. Elmas, C. Fouassier, P. Hagemuller, *Phys. B+C* **1980**, 99, 81.
- [24] T. Song, L. Chen, D. Gastol, B. Dong, J. F. Marco, F. Berry, P. Slater, D. Reed, E. Kendrick, *Chem. Mater.* **2022**, 34, 4153.
- [25] N. Yabuuchi, M. Kajiyama, J. Iwatate, H. Nishikawa, S. Hitomi, R. Okuyama, R. Usui, Y. Yamada, S. Komaba, *Nat. Mater.* **2012**, 11, 512.
- [26] Z.-X. Huang, X.-L. Zhang, X.-X. Zhao, Y.-L. Heng, T. Wang, H. Geng, X.-L. Wu, *Sci. China Mater.* **2022**, 66, 79.
- [27] C.-Y. Yu, J.-S. Park, H.-G. Jung, K.-Y. Chung, D. Aurbach, Y.-K. Sun, S.-T. Myung, *Energy Environ. Sci.* **2015**, 8, 2019.
- [28] J.-J. Ding, Y.-N. Zhou, Q. Sun, Z.-W. Fu, *Electrochem. Commun.* **2012**, 22, 85.
- [29] J. Meng, J. Liang, M. Liang, W. Li, C. Lin, X. Ke, Z. Shi, L. Liu, *Sci. China Mater.* **2023**, 66, 3445.
- [30] S.-H. Bo, X. Li, A. J. Toumar, G. Ceder, *Chem. Mater.* **2016**, 28, 1419.
- [31] K. Kubota, I. Ikeuchi, T. Nakayama, C. Takei, N. Yabuuchi, H. Shiiba, M. Nakayama, S. Komaba, *J. Phys. Chem. C* **2015**, 119, 166.
- [32] W. Ko, M.-K. Cho, J. Kang, H. Park, J. Ahn, Y. Lee, S. Lee, S. Lee, K. Heo, J. Hong, J.-K. Yoo, J. Kim, *Energy Storage Mater.* **2022**, 46, 289.
- [33] W. Park, M. G. T. Nathan, S. C. Han, J.-W. Lee, K.-S. Sohn, M. Pyo, *RSC Adv.* **2020**, 10, 43273.
- [34] L. Zheng, J. C. Bennett, M. N. Obrovac, *J. Electrochem. Soc.* **2019**, 166, A2058.
- [35] S. Wang, F. Chen, H.-Y. He, Y.-R. Zhu, H.-B. Liu, C.-H. Chen, *J. Alloys Compd.* **2022**, 925, 166690.
- [36] C. Ma, X.-L. Li, X.-Y. Yue, J. Bao, R.-J. Luo, Y.-N. Zhou, *Chem. Eng. J.* **2022**, 432, 134305.
- [37] W. Li, Y. Wang, G. Hu, Z. Peng, Y. Cao, Y. Zeng, K. Du, *J. Alloys Compd.* **2019**, 779, 147.
- [38] Y. Wang, P. Cui, W. Zhu, Z. Feng, M.-J. Vigeant, H. Demers, A. Guerfi, K. Zaghib, *J. Power Sources* **2019**, 435, 226760.
- [39] S. Chu, D. Kim, G. Choi, C. Zhang, H. Li, W. K. Pang, Y. Fan, A. M. D'Angelo, S. Guo, H. Zhou, *Angew. Chem., Int. Ed.* **2023**, 12, e202216174.

- [40] I. Lee, G. Oh, S. Lee, T.-Y. Yu, M. H. Alfaruqi, V. Mathew, B. Sambandam, Y.-K. Sun, J.-Y. Hwang, J. Kim, *Energy Storage Mater.* **2021**, 41, 183.
- [41] Y. Wang, R. Xiao, Y.-S. Hu, M. Avdeev, L. Chen, *Nat. Commun.* **2015**, 6, 6954.
- [42] X.-G. Yuan, Y.-J. Guo, L. Gan, X.-A. Yang, W.-H. He, X.-S. Zhang, Y.-X. Yin, S. Xin, H.-R. Yao, Z. Huang, Y.-G. Guo, *Adv. Funct. Mater.* **2022**, 32, 211466.
- [43] E. M. Garcia, *Surf. Coat. Technol.* **2013**, 235, 10.
- [44] B. Sambandam, M. H. Alfaruqi, S. Park, S. Lee, S. Kim, J. Lee, V. Mathew, J.-Y. Hwang, J. Kim, *ACS Appl. Mater. Interfaces* **2021**, 13, 53877.
- [45] S. Chu, C. Zhang, H. Xu, S. Guo, P. Wang, H. Zhou, *Angew. Chem. Int. Ed.* **2021**, 60, 13366.
- [46] Y. Jeong, H.-J. Shin, G. Oh, M. H. Alfaruqi, M. S. Ahmed, V. Mathew, H.-G. Jung, J. Kim, J.-Y. Hwang, *J. Mater. Chem. A* **2022**, 10, 18050.
- [47] F. Yu, T. Huang, P. Zhang, Y. Tao, F.-Z. Cui, Q. Xie, S. Yao, F. Wang, *Energy Storage Mater.* **2019**, 22, 235.
- [48] J.-Y. Hwang, S.-T. Myung, J. U. Choi, C. S. Yoon, H. Yashiro, Y.-K. Sun, *J. Mater. Chem. A* **2017**, 5, 23671.
- [49] S. Chu, D. Kim, G. Choi, C. Zhang, H. Li, W. K. Pang, Y. Fan, A. M. D'Angelo, S. Guo, H. Zhou, *Angew. Chem.* **2023**, 135, e202216174.
- [50] C. L. Jakobsen, B. P. Andersen, M. Johansen, C. K. Christensen, A. O. Drejer, M. A. Karlsen, D. B. Ravnsbaek, *J. Power Sources* **2024**, 591, 233875.
- [51] S. Komaba, C. Takei, T. Nakayama, A. Ogata, N. Yabuuchi, *Electrochem. Commun.* **2010**, 12, 355.
- [52] M. Tromp, J. Moulin, G. Reid, J. Evans, *AIP Conf. Proc.* **2017**, 882, 699.
- [53] Y.-N. Zhou, J.-J. Ding, K. W. Nam, X. Yu, S.-M. Bak, E. Hu, J. Liu, J. Bai, H. Li, Z.-W. Fu, X.-Q. Yang, *J. Mater. Chem. A* **2013**, 1, 11130.
- [54] X. Xia, J. R. Dahn, *Electrochem. Solid-State Lett.* **2011**, 15, A1.
- [55] S.-M. Oh, S.-T. Myung, J.-Y. Hwang, B. Scrosati, K. Amine, Y.-K. Sun, *Chem. Mater.* **2014**, 26, 6165.
- [56] J.-Y. Hwang, S.-T. Myung, C. S. Yoon, S.-S. Kim, D. Aurbach, Y.-K. Sun, *Adv. Funct. Mater.* **2016**, 26, 8083.
- [57] G. Kresse, J. Furthmüller, *Phys. Rev. B* **1996**, 54, 11169.
- [58] P. E. Blöchl, *Phys. Rev. B* **1994**, 50, 17953.
- [59] S. Kansara, H. Kang, S. Ryu, H. H. Sun, J.-Y. Hwang, *J. Mater. Chem. A* **2023**, 11, 24482.
- [60] J. Wei, L. Shaw, W. Chen, *Phys. Rev. Mater.* **2022**, 6, 095403.